

Constraints on the dense matter equation of state from young and cold isolated neutron stars

Received: 13 September 2023

A. Marino  , C. Dehman  , K. Kovlakas  , N. Rea  , J. A. Pons  & D. Viganò 

Accepted: 9 May 2024

Published online: 20 June 2024

 Check for updates

Neutron stars are the dense and highly magnetic relics of supernova explosions of massive stars. The quest to constrain the equation of state (EOS) of ultradense matter and thereby probe the behaviour of matter inside neutron stars is one of the core goals of modern physics and astrophysics. A promising method involves investigating the long-term cooling of neutron stars, comparing theoretical predictions with various sources at different ages. However, limited observational data, and uncertainties in source ages and distances, have hindered this approach. Here, by re-analysing XMM-Newton and Chandra data from dozens of thermally emitting isolated neutron stars, we have identified three sources with unexpectedly cold surface temperatures for their young ages. To investigate these anomalies, we conducted magneto-thermal simulations across diverse mass and magnetic fields, considering three different EOSs. We found that the 'minimal' cooling model failed to explain the observations, regardless of the mass and the magnetic field, as validated by a machine learning classification method. The existence of these young cold neutron stars suggests that any dense matter EOS must be compatible with a fast cooling process at least in certain mass ranges, eliminating a significant portion of current EOS options according to recent meta-modelling analysis.

Neutron stars are incredibly dense objects with densities several times that of atomic nuclei ($\rho \approx 10^{14}$ g cm $^{-3}$). They hold unique information about the properties and behaviour of matter under extreme conditions of densities and magnetic fields^{1–3}. Their internal structure, mass-radius relationship and overall behaviour relies on a unique equation of state (EOS), which describes the relationship between pressure, density and composition, in a regime unreachable in Earth laboratories. The EOS not only determines the structure, cooling rates and rotational properties of neutron stars but also has a role in astrophysical phenomena such as gravitational wave signals emitted during mergers with other neutron stars or black holes. Deciphering the actual EOS of dense matter is a key open question for several branches of physics.

Constraining the dense matter EOS involves the combination of various theoretical models, computational techniques and astrophysical observations, all aimed at refining and validating our understanding through the comparison of theoretical predictions with observational data. The interactions between particles, such as neutrons, protons and electrons, are crucial factors that shape the EOS at different density regimes, as are the superfluid components. Furthermore, as densities increase towards the core of the star, the nature of matter within neutron stars becomes more uncertain, with the possible appearance of exotic particles such as hyperons, meson condensates or quark matter⁴.

Neutron-star cooling is caused by a combination of neutrino emission from the dense core of the star and thermal photons emitted

¹Institute of Space Sciences (ICE), CSIC, Barcelona, Spain. ²Institut d'Estudis Espacials de Catalunya (IEEC), Castelldefels (Barcelona), Spain. ³Departament de Física Aplicada, Universitat d'Alacant, Alacant, Spain.  e-mail: marino@ice.csic.es; dehman@ice.csic.es; kovlakas@ice.csic.es; rea@ice.csic.es

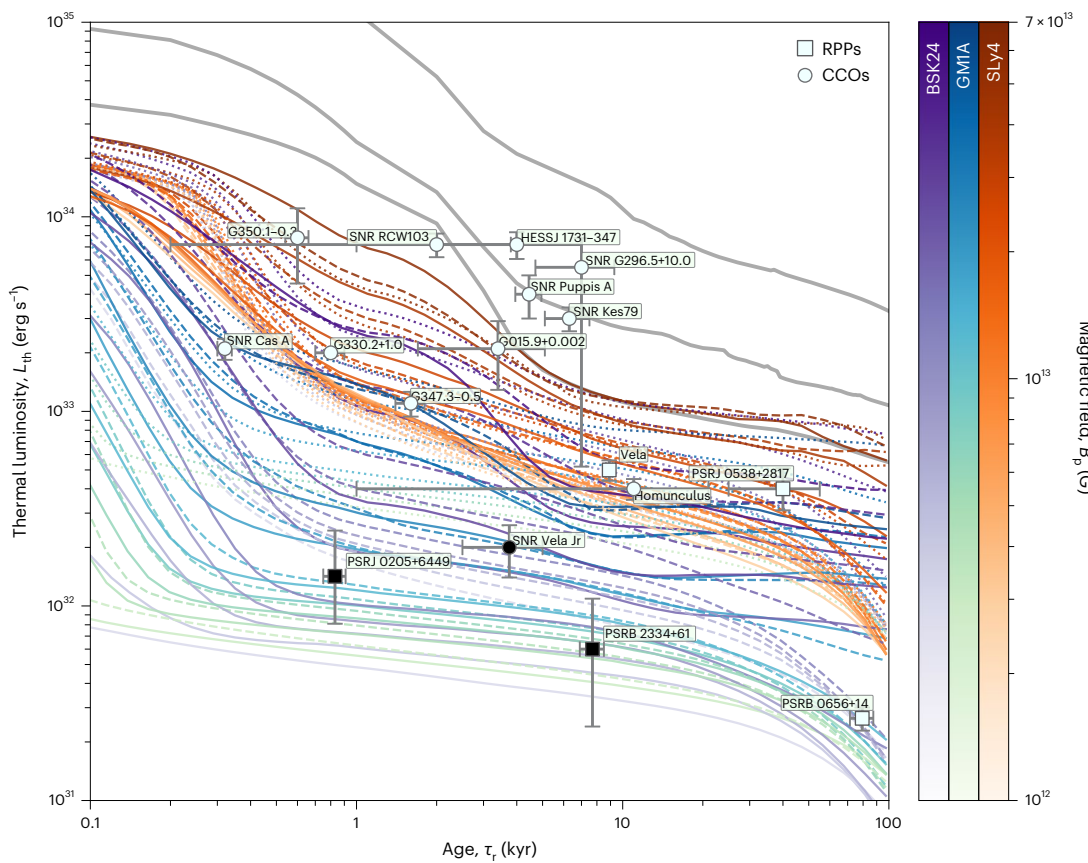


Fig. 1 | Comparison between observational data and theoretical cooling curves.

Observations. The surface thermal luminosity (L_{th}) is plotted as a function of the real age (τ_r) for data and models. Observations include RPPs (squares) and CCOs (circles), with the three sources studied in this work in black. The 81 cooling curves used in our analysis are coloured based on their EOS: SLy4, orange; BSK24, purple; GM1A, blue. The line styles denote the masses: $1.4 M_{\odot}$, dots; $1.6 M_{\odot}$, dashed lines;

$1.8 M_{\odot}$, solid lines. The colour bars show the dipolar magnetic field values which were in the range of $B_p = 1 \times 10^{12} - 70 \times 10^{12}$ G. Only for comparison, we also show three grey curves corresponding to stronger magnetic-field intensities of 10^{14} G, 3×10^{14} G and 10^{15} G, not used in our statistical analysis. Errors in the luminosities are calculated as described in Methods.

from the outer layers. By measuring the surface temperatures of many objects over a large age range, neutron-star cooling models (and consequently, the EOS) can be constrained⁵. The cooling history of a neutron star involves multiple parameters apart from the EOS, leading to diverse tracks for neutron stars born with different initial conditions, such as the object mass, the envelope composition and the initial magnetic field.

Cooling curves were historically divided into two theoretical classes: (1) the ‘standard’ or ‘minimal’ cooling ones, dominated by modified Urca processes possibly with the addition of superconductivity or superfluidity in the core producing neutrino cooling via Cooper pairs⁶; and (2) those showing ‘enhanced cooling’ due to the activation of direct Urca processes, hyperons, or even quark matter or meson condensates^{7,8}.

Evidences for the presence of enhanced cooling were presented for some isolated neutron stars^{5,9–12} and for transiently accreting neutron stars^{13–17}. Both scenarios can provide independent constraints on the neutron-star cooling. However, on one side, the lack of well-constrained spectral energy distributions, exact ages and/or precise distances, and, on the other side, uncertainties on the accretion state and history precluded any firm and conclusive constraint on the EOS. Furthermore, it was suggested¹⁸ that the dissipation of the magnetic field in the highly resistive crust could hide the effect of the enhanced cooling mechanisms for stars with magnetic fields above 10^{14} G. In this Article, we present a detailed study of three extremely cold, young and close-by neutron stars, the mere existence of which is constraining the neutron-star EOS because the ‘enhanced’ cooling processes are required to reconcile the models with the observational data.

To perform a systematic study of surface temperatures in isolated neutron stars across different classes, we re-analysed deep XMM-Newton and/or Chandra data for a sample of 70 isolated neutron stars. Such a sample consists of sources with a statistically significant spectral contribution by a thermal component and with a reliable and sufficiently well-known age and distance (C.D. et al., manuscript in preparation). Out of this sample, three sources stood out for being colder by about an order of magnitude with respect to the other objects at similar young ages (Extended Data Tables 1–3). These sources are two rotation-powered pulsars (RPPs) PSR J0205+6449 (spin perio $P = 70$ ms, surface dipolar magnetic field $B_p = 7 \times 10^{12}$ G and age $\tau_r = 841$ yr (ref. 19)) and PSR B2334+61 ($P = 490$ ms, $B_p = 2 \times 10^{13}$ G and $\tau_r = 7,700$ yr (ref. 20)), and a central compact object (CCO), CXOU J0852–4617 (age = 2,500–5,000 yr (ref. 21)). All three objects have an associated supernova remnant studied at all wavelengths, providing precise distance and age constraints (in the case of PSR J0205+6449, also the historical record of its associated supernova, SN 1118; Methods). For each source, we estimated the effective blackbody temperature and the radius of the emitting surface through X-ray spectral analysis and used these values to calculate their thermal luminosity. We used simple blackbody models (Extended Data Fig. 1 and Extended Data Table 2), but checked that our final results held using more sophisticated atmosphere models (Extended Data Table 4) and considering the presence of an additional ‘hidden’ thermal contribution by the whole neutron-star surface (Methods and Extended Data Figs. 2 and 3). In Fig. 1, we report on the thermal luminosities of all the RPPs and CCOs with a precise estimate of the age and distance, the former not relying on the characteristic

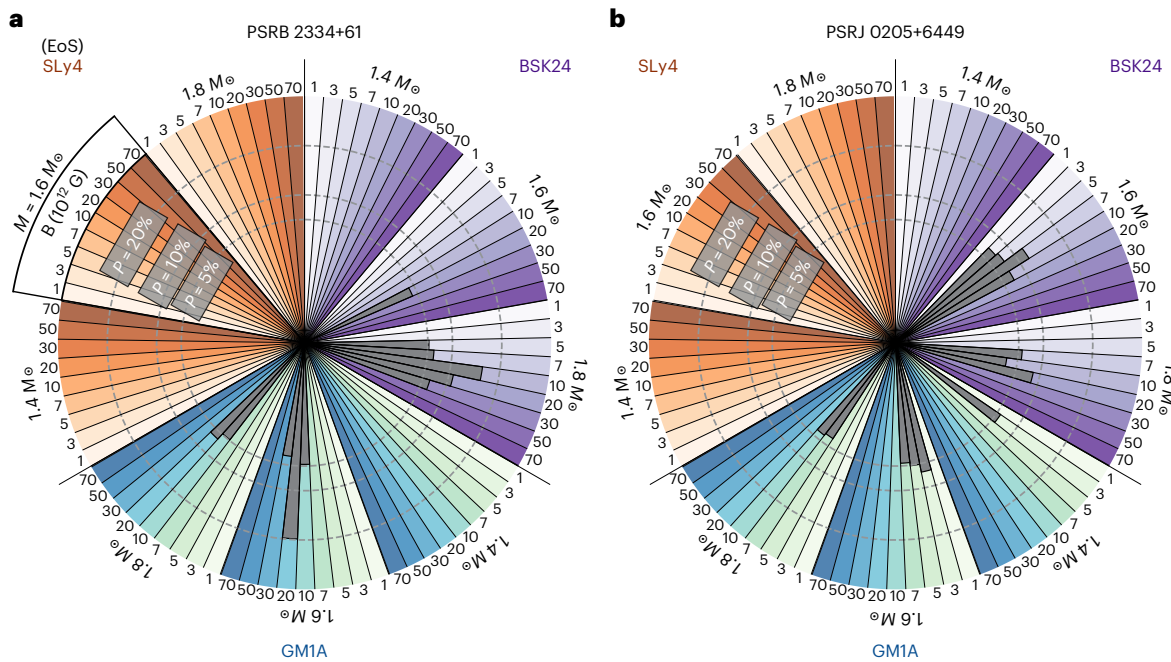


Fig. 2 | Pie chart of our 4D classification method. We report the results of the classification method for PSR B2334+61 (a) and PSR J0205+6449 (b). Each chart is divided in three sectors for each of the EOS used: BSK24, purple; SLy4, orange;

GM1A, blue. Each sector is further broken down by mass and magnetic field. Superimposed to the cloves, grey histograms denote the posterior probability for each simulation clove to be the cooling curve followed by the source.

age of the pulsar inferred from the timing analysis (which is known to have large uncertainties). Being so young, that is, with ages between 800 yr and 8,000 yr, and yet so cold, PSR J0205+6449, PSR B2334+61 and CXOU J0852–4617 must have necessarily experienced some sort of rapid cooling.

To comprehend why the thermal X-ray luminosity appears significantly faint during the early stages of these three objects, we conducted magneto-thermal simulations^{22–24} exploring different EOSs, masses and a range of magnetic fields. In particular, our collection of 81 simulations comprises three distinct EOSs with various cooling channels, including modified Urca, Cooper pairs and direct Urca (among other channels; see, for example, ref. 11). In particular, SLy4²⁵ assumes a standard ‘minimal’ cooling scenario and does not activate ‘enhanced cooling’ processes, whereas BSK24²⁶ and GM1A^{27–29}, for certain masses, do involve ‘enhanced cooling’ processes such as nucleon direct Urca and hyperons direct Urca (the latter activated only for the GM1A).

In addition, we considered 3 different masses ($1.4 M_{\odot}$, $1.6 M_{\odot}$ and $1.8 M_{\odot}$), along with 9 initial magnetic-field values for the surface dipolar field ranging from $1 \times 10^{12} G$ to $7 \times 10^{13} G$ at the pole, with no toroidal magnetic field to avoid Joule heating and focus on the cold neutron-star scenario. Furthermore, we solely employed an iron-envelope model, as alternative compositions containing light elements would predict at these ages a thermal luminosity approximately one order of magnitude brighter than that projected by the iron-envelope model³⁰ (Methods and Extended Data Fig. 4).

In Fig. 1, we show the observational measurements compared with the magneto-thermal evolutionary tracks. Even at first glance, it is clear that some of the explored scenarios are not matching the faint thermal luminosities of these extremely cold sources. Indeed, assuming a SLy4 EOS, the dramatic drop in surface temperature in the three outliers could not be reached for any combination of mass and magnetic fields. In the exotic case of having hyperons in the core, namely, the case of GM1A, the cooling might proceed fast enough to be compatible with the observational data. However, for the BSK24 EOS, when the mass is larger than $1.6 M_{\odot}$ direct Urca is activated and the tracks show an enhanced cooling compatible with the data. Following a less qualitative

and more rigorous approach, we used machine learning (Methods) to find the range of parameters that better described each source. At that aim, we first considered the observational data and the simulations in a three-dimensional (3D) space considering as independent parameters the thermal luminosity L_{th} , spin period P and spin derivative \dot{P} . We then also extended these simulations into a four-dimensional (4D) space, including also the age of the sources. As for the CCO CXOU J0852–4617, P and \dot{P} are unknown, this analysis was carried out for only the two RPPs. The extension to a 4D space allowed us to check whether curves that may explain the observed L_{th} would also predict P and/or \dot{P} compatible with the timing parameters of the sources at the same age.

In Fig. 2, we summarize the results of our machine learning simulations in 4D (the results of the 3D are very similar; Methods, Extended Data Table 5 and Extended Data Fig. 5). According to these methods, we can quantitatively exclude the EOS without a physical mechanism to activate an enhanced cooling at young age (in our set of EOSs, this would correspond to SLy4).

In particular, for PSR B2334+61 all cooling curves point towards the source having a relatively high mass ($\sim 1.6 M_{\odot}$) and a dipolar magnetic field at birth of $\sim 0.7 \times 10^{13}$ – $3 \times 10^{13} G$, compatible with its current value. Despite a slight preference is visible for the hyperon EOS (GM1A) for this pulsar, we caveat that more simulations with other enhanced-cooling EOSs might also reach similar probabilities; hence, at this stage, we cannot constrain the exact EOS with this technique. Applying these methods to PSR J0205+6449, we find that both enhanced-cooling EOSs, BSK24 and GM1A, with masses of $\sim 1.6 M_{\odot}$ are compatible with its observed parameters, resulting in an initial magnetic field within $\sim 3 \times 10^{12}$ – $20 \times 10^{12} G$, again in agreement with the estimated value for this pulsar. For both sources, the simulations with the SLy4 EOS considering only ‘minimal’ cooling for any set of parameters provide a non-acceptable match with the data (probabilities $< 5\%$; Methods). Furthermore, considering only the source thermal luminosity and age, this conclusion holds also for CXOU J0852–4617.

Given the uniqueness of the EOS, these results provide evidence that neutron stars cannot be governed by an EOS that is not compatible with the low luminosities of PSR J0205+6449, PSR B2334+61 and

CXOU J0852–4617, at least in a certain mass range. The precise error determinations, the updated values for the distances and/or the ages of these three sources, along with the machine learning approach used to corroborate our conclusions, make these results the strongest measurement up to now in favour of enhanced cooling. We found that only EOSs (and compositions) allowing a fast cooling process in the first few thousand years can be successfully reconciled with the thermal emission of all sources in our sample. Although a detailed and comprehensive analysis of various possibilities for fast cooling (for example, hyperons, quarks, pure nucleonic matter with very large symmetry energy) is beyond the scope of this paper, the issue itself stimulates thought. In particular, considering a simplified nucleonic meta-modelling³¹, the proposed EOS that does not have a high enough proton fraction to activate fast cooling processes for any reasonable neutron-star mass is estimated to be about 75%. This modelling, despite being simplified and dependent on the assumed composition, shows that a significant fraction of the currently available EOSs are potentially excluded by the mere existence of these cold and young neutron stars.

Methods

Source sample

In this work, we present the analysis of deep X-ray observations of three neutron stars, PSR J0205+6449, PSR B2334+61 and CXOU J0852–4617, as part of a larger work done on the re-analysis of a total of 70 isolated thermally emitting neutron stars (C.D. et al., manuscript in preparation). The former two sources are young radio pulsars, the emissions of which are directly powered by their rotational energy, so that they are classified as RPPs. CXOU J0852–4617 is instead a non-pulsating neutron star classified as a CCO, a class of isolated neutron stars localized in the geometrical centre of their supernova remnant (SNR). A summary of their timing parameters, the available X-ray observations and all relevant references are presented in the Extended Data Tables 1 and 3.

All neutron stars in our sample are associated with an SNR. PSR J0205+6449 is associated with the pulsar wind nebula 3C 58 and with the SNRG130.7+3.1, and it is emitting from radio to gamma-rays^{32,33}. The other pulsar in the sample, PSR B2334+61, is also associated with an SNR, that is, with SNR G114.3+0.3³⁴, and it is detected in radio and X-rays. The CCO CXOU J0852–4617 is the X-ray bright point-source lying only ~35 arcsec away³⁵ from the geometrical centre of the shell-type SNR G266.2–1.2, also known as Vela Jr³⁶. As for many other CCOs, it does not have detected pulsations, but its faint optical magnitude limits, lack of variability and X-ray spectral properties confirm its neutron-star nature³⁷. Interestingly, CXOU J0852–4617 is one of the very few CCOs that might have been observed in a different waveband than the X-ray. A candidate faint point-like infrared counterpart for the source has been found with European Southern Observatory Very Large Telescope (ESO-VLT) observations^{35,38} and interpreted as emission from the neutron-star magnetosphere or from a relic disk around the CCO. None of the three sources showed any variability in our data (nor in the past), as it is indeed expected for an isolated neutron star with a relatively low magnetic field.

Distances and real-age constraints

The location on the luminosity–age plane (Fig. 1) is critically dependent on the accuracy with which we know both the distance and the age of our sources. In the three sources we report here, the SNRs and H I regions around the objects were studied in great detail, providing robust measurements of distances and ages.

PSR J0205+6449 is considered one of the youngest pulsars known. The source has been proposed to be the leftover of the historical supernova SN 1181, providing an age of 839 yr. However, several elements, such as the measured expansion speeds of both the synchrotron bubble and of the thermal filaments³⁹, initially suggested that PSR J0205+6449 (and 3C 58) may be instead older by thousands of years than SN 1181. Note that even in the unlikely case that PSR J0205+6449 is older than

SN 1181, an upper limit on its age can be posed using its characteristic age τ_c of 54 kyr. Even assuming this upper limit, the SLy4 curves cannot explain its luminosity. Its distance was originally estimated to be 3.2 kpc (ref. 40). More recent H I measurements have instead placed the source at a closer distance of just 2 kpc (refs. 19,41). This is in-line with the association with SN 1181 and compatible with the source proper motion⁴². It is noteworthy, however, that the results of this paper would hold even assuming the outdated distance of 3.2 kpc, as the corresponding increase in luminosity would still place PSR J0205+6449 at a value of $\lesssim 10^{33}$ erg s⁻¹, that is, lower than the cooling curves simulated with SLy4.

For PSR B2334+61 instead, a distance range of 2.1–3.3 kpc was reported by several authors^{43,44} according to its radio dispersion measure. In the following we adopt those values. It is noteworthy that this result has been recently challenged by observations of the H I line in the SNR G114.3+0.3, according to which the source (and its SNR) is placed at a much closer location, that is at 700 pc (ref. 20). In addition, a 0.1–0.9 kpc range was reported by ref. 41 on the basis of kinematic analysis. Note that if this distance is assumed the pulsar would be even colder, hence our conclusions will not change. A value of 7.7 kyr was estimated for the real age of the source from the study of the SNR²⁰ (while its characteristic age is τ_c is 40 kyr). The real age of PSR B2334+61 has been reported without any uncertainty. We therefore adopted a 10% relative error on this value throughout this paper. For consistency, we also used a 10% uncertainty for the age of PSR J0205+6449, which is lacking of uncertainties as well as it coincides with the historical date of SN 1181.

Finally, CXOU J0852–4617 is associated with the SNR Vela Jr (for a critical discussion on the topic, see ref. 37). Several arguments, including its expansion rate, the estimated shock speed and its association with the Vela Molecular Ridge (see, for a review, ref. 21), suggest that the CXOU J0852–4617 distance lies in the 0.5–1.0 kpc range, and its real age would lie in the range 2.5–5.0 kyr (ref. 21).

Data reduction

In this work, we considered only XMM-Newton and Chandra observations^{37,44,45}, being those providing the most accurate X-ray spectral energy distributions. Details on all observations can be found in Extended Data Table 3.

PSR J0205+6449 and its nebula 3C 58 have been observed three times by Chandra between 2001 and 2003⁴⁵. PSR B2334+61 has been observed only once by XMM-Newton⁴⁴. However, many archival XMM-Newton and Chandra observations are available for CXOU J0852–4617³⁷. For the latter, we analysed only the Chandra observation with the longest exposure time, and for which the Advanced CCD Imaging Spectrometer ACIS-S has been employed. We used only the Chandra data to excise more effectively any contribution from the underlying SNR.

In the following subsections, we describe the data reduction procedure followed for all the datasets used in this work.

XMM-Newton

We include data from the EPIC-pn detector⁴⁶ onboard XMM-Newton. For all the observations, the EPIC-pn was set in small-window mode (time resolution of 5.7 ms). Data reprocessing was performed with the XMM-Newton Science Analysis Software (SAS) v. 20.0.0. To reduce the data, we first filtered the event files for periods of high background activity. We used the EPATPLOT tool to display the observed pattern distribution versus the expected one and thereby assess the pile-up impact, finding that it was negligible for all the observations considered here. The source counts were extracted from a circle of 20 arcsec radius centred on the coordinates of the source. For the background, we used a region of the same size and shape, located sufficiently far from the source.

Chandra

All three Chandra observations of PSR J0205+6449 and the single observation of CXOU J0852–4617 used here were carried out using

the ACIS-S. Data processing, reduction and spectral extraction of all observations was performed within CIAO v.4.14 using the standard pipelines. A 3×3 pixel square box was used to identify source photons, small enough to limit contamination from the surrounding nebula, following standard approaches⁴⁵. A region of the same size, but located far from the source and 3C 58 was used for the background. The routine SPECEXTRACT task was used to build the spectra and create the ancillary response and the redistribution matrix files.

Spectral analysis

The spectral analysis was performed using XSPEC v.12.12.1. For PSR J0205+6449 and CXOU J0852–4617, the spectra were grouped in order to have at least 20 counts per bin, enabling use of the χ^2 statistics. The low count-rate of the PSR B2334+61 observation forced us to choose a different grouping strategy, 10 counts per bin, and consider the C statistics instead. We kept data only within an energy interval where the source data points were higher than the background level, thereby selecting 0.3–10 keV, 0.5–2 keV and 0.5–4.5 keV for PSR J0205+6449, PSR B2334+61 and CXOU J0852–4617, respectively. In all the models used to describe the data, we included the TBABS component to take into account the effect of the interstellar absorption, setting the photoelectric cross-sections to the values provided by ref. 47. For the elemental abundances, we tried the tables by both refs. 48,49, finding negligible differences.

While the spectral shapes of PSR B2334+61 and CXOU J0852–4617 were relatively simple, being consistent with a single, thermal component, the spectrum of PSR J0205+6449 is apparently dominated by a power-law component. Details on the results of the fits are reported in Extended Data Table 2, and we refer to Extended Data Fig. 1 for a plot with spectra, best-fit models and corresponding residuals.

For PSR J0205+6449, we initially used a simple POWERLAW model to describe the three available Chandra spectra, finding an already acceptable fit ($\chi^2/\text{d.f.} = 587/600$). We then added a blackbody component, described with the BBODYRAD model in XSPEC. The parameters of BBODYRAD are the blackbody temperature kT_{bb} and its normalization K_{bb} , which translates into the blackbody radius R_{bb} by means of the formula $K_{\text{bb}} = (R_{\text{bb}}/D_{10\text{kpc}})^2$, with $D_{10\text{kpc}}$ the distance of the source in units of 10 kpc. Adding a blackbody component, results in a slight improvement in the fit, which turns out to be highly significant when we use the ref. 49 abundances for the hydrogen column density, N_{H} , whereas only marginally significant with the ref. 48 abundances, with probability of improvement by chance of $\sim 10^{-7}$ and $\sim 10^{-3}$, estimated using FTEST. Such a result indicates the clear presence of correlation between N_{H} and the blackbody parameters. To further investigate the significance of the thermal component in the fit with the ref. 48 abundances, we applied the Goodman–Weare algorithm of Markov chain Monte Carlo⁵⁰ to produce contour plots for N_{H} , the surface temperature kT_{bb} and the blackbody radius R_{bb} . We used 20 walkers and a chain length of 5×10^5 , to calculate the marginal posterior distributions of the best-fit parameters for all three Chandra spectra. The results are presented in the corner plot in Supplementary Fig. 1. As evident, both kT_{bb} and K_{bb} can be sufficiently constrained and the normalization is small, but still not consistent with zero. Such a result confirms the presence of a thermal component in the emission of PSR J0205+6449, in agreement with the results from previous studies of the source where the thermal emission was indeed significantly detected⁴⁵.

To describe the emission by PSR B2334+61, we tried both a BBODYRAD model or a single POWERLAW. Despite providing a statistically acceptable fit, the latter model requires a very soft power-law component, with $\Gamma > 6$, which is unphysical and suggests that the power-law component is actually mimicking a blackbody-like spectrum. We therefore use a simple BBODYRAD model (similar to ref. 44), which is also sufficient to describe the spectrum of this source, CXOU J0852–4617, as also reported by other authors³⁷. The best-fit

models and relative residuals for these sources are shown in Extended Data Table 2 and Extended Data Fig. 1. According to these fits, the thermal emissions from PSR J0205+6449 and PSR B2334+61 are both consistent with blackbody temperatures of 0.15–0.25 keV (with the former slightly hotter) arising from hotspots of size 1–2 km. Interestingly, CXOU J0852–4617 is instead characterized by a significantly hotter blackbody temperature, that is, around 0.4 keV, and smaller size, about 0.2–0.3 km. The results of the fits are consistent, within the errors, with studies using the same datasets and absorbed blackbody models^{37,44,45}.

Once the best-fit models were found, we applied the convolution model CFLUX to the BBODYRAD component to estimate the bolometric flux that can be considered purely thermal. These results are reported in Extended Data Table 2.

We then used the source distances to estimate their thermal luminosity following standard propagation errors techniques. In the following, we refer to this as observed luminosity L_{obs} . However, for our statistical analysis, we estimated the error distribution for PSR J0205+6449 and PSR B2334+61 using a more rigorous approach that involves Monte Carlo uncertainty propagation (see below). The luminosity obtained with this technique, L_{stat} from now on, is always well compatible within the errors with L_{obs} . Both values are reported in Supplementary Table 1.

Testing atmosphere models

In this work, we have used systematically a simple blackbody model to describe the thermal emission from these sources. Despite its success in describing the spectra from several isolated neutron stars and its simplicity, this approach ignores some crucial details on the underlying physics of neutron-star emission: the possible presence of an atmosphere that modifies the blackbody emission coming from the neutron-star surface through Compton scattering and other radiative processes. Several studies have shown that when the thermal component is modelled using a proper model for the neutron-star atmosphere instead of a blackbody model, as in the case of Cassiopeia A^{9,51}, a different set of parameters could be obtained, although at the expense of assuming certain densities and compositions, which are typically unknown. To check whether our results would change when adopting atmosphere models, we have fitted our three sources with NSMAXG⁹, which is suited to probe different chemical compositions (H, C, O) and different magnetic-field intensities. We first tried to fix the normalization N_{nsmaxg} , which is connected to the radius of the emitting region with the formula $N_{\text{nsmaxg}} = (R_{\text{em}}/R_{\text{NS}})^2$, to 1, corresponding to the case where the whole surface emits (where R_{em} is the emitting radius and R_{NS} is the neutron star radius). However, the resulting fits were unacceptable, so we left N_{nsmaxg} free to vary, finding always values lower than 1. We also fixed the distances to the values reported in Extended Data Table 1. For all sources, we explored the case of $B = 10^{12}$ G and tried as chemical compositions H, C and O. For the two RPPs, we found that all the probed chemical compositions could lead to equally acceptable fits with respect to the simple blackbody models. For CXOU J0852–4617, however, only the model with H was compatible with the data. Finally, once the best-fit parameters were obtained, we used again CFLUX to estimate the bolometric flux. We report the final parameters in Extended Data Table 4. From a comparison between the results with a simple blackbody model (Extended Data Table 2), we find that indeed adopting more physically motivated models of the neutron-star surface emission leads to different best-fit values for the effective temperatures and the sizes of the emitting regions. Nevertheless, using an atmosphere model leads in all cases to bolometric fluxes that are systematically smaller or at least compatible within the errors with respect to the fluxes estimated through a simple blackbody model. These tests show that the low thermal luminosities reported in this paper might even represent an overestimate of the actual thermal luminosity from these sources, solidifying our conclusions.

Adding the hidden contribution from the whole neutron-star surface

The thermal components detected in all these sources are characterized by blackbody radii of a few kilometres or less and can be therefore considered as being radiated by hotspots on the neutron-star surface. However, a contribution from the entire neutron-star surface at lower temperature, that is, in an energy range where interstellar absorption is stronger, can not be excluded *a priori*. We therefore tried to estimate the upper limit of this hidden contribution by adding to our final fits an additional blackbody component with radius fixed to the neutron-star assumed radius (in our case, a value of 11 km (ref. 52) was chosen). The temperature of this blackbody component was used to estimate an upper limit on the thermal luminosity from the entire surface, L_{surf} , hereafter.

We show both the best fit and the upper limit of a possible undetected surface blackbody thermal component in Extended Data Fig. 2, showing how even if actually present, the latter emission is always made undetectable by interstellar extinction. For all sources, these upper limits, reported in Supplementary Table 1, are still too low to reconcile these sources with the cooling tracks simulated with the SLy4 EOS, as shown in Extended Data Fig. 3. In the same figure, we also show the upper limits considering the maximum flux across all models (the three atmosphere models and the adopted blackbody model).

Magneto-thermal simulations

Our astrophysical scenario of interest is the long-term evolution of magnetic fields in neutron stars. In the crust of a neutron star, the evolution of the system is governed by two coupled evolution equations: the induction equation and the heat diffusion equation (see the review by ref. 53 for more details), given by:

$$\frac{\partial \mathbf{B}}{\partial t} = -\nabla \times \left[\eta(T) \nabla \times (e^v \mathbf{B}) + \frac{c}{4\pi n_e} [\nabla \times (e^v \mathbf{B})] \times \mathbf{B} \right], \quad (1)$$

$$c_V(T) \frac{\partial(T e^v)}{\partial t} = \nabla \cdot (e^v \kappa(T, \mathbf{B}) \cdot \nabla(e^v T)) + e^{2v} (Q_J(\mathbf{B}, T) - Q_v(\mathbf{B}, T)), \quad (2)$$

where \mathbf{B} is the magnetic field vector, T the surface temperature, t is the time, c is the speed of light, e is the elementary electric charge, n_e is the electron number density, $\eta(T) = c^2/(4\pi\sigma_e(T))$ is the magnetic diffusivity (inversely proportional to the electrical conductivity σ_e), c_V is the heat capacity per unit volume, κ is the anisotropic thermal conductivity tensor, Q_J and Q_v are the Joule heating rate and neutrino emissivity per unit volume, respectively, and e^v is the relativistic redshift correction.

The interconnections between the magnetic and thermal evolution equations occur at the microphysical level. On the one hand, as the temperature decreases due to neutrino emission, the resistivity of the matter also decreases, leading to increased thermal and electric conductivities. At sufficiently low temperatures, these conductivities become temperature independent¹⁸, resulting in a gradual decrease in the ohmic dissipation rate. On the other hand, as the magnetic field evolves, it affects the thermal conductivity both along and across the magnetic-field lines, influencing the local temperature. This, in turn, causes significant variations in the surface temperature distribution T_s , which can be observed and constrained through measurements. Simultaneously, the Hall effect drives electric currents towards the crust/core boundary, where the presence of high impurities and pasta phases facilitates a more efficient dissipation of the magnetic field⁵⁴. Consequently, the magnetic energy is converted into Joule heating Q_J . While the Hall effect itself does not directly dissipate magnetic energy, it gives rise to small-scale magnetic structures where ohmic dissipation is enhanced. To a lesser extent, the magnetic field \mathbf{B} also influences c_V and Q_v .

As the induction equation and the heat diffusion equation are coupled at a microphysical level, they must be supplemented by an EOS, which allows to build the background model of the neutron star solving the Tolman–Oppenheimer–Volkov equations using different models of a nuclear EOS at zero temperature (which we take from the online public database CompOSE <https://compose.obspm.fr/>). At the temperatures ($T < 10^{10}$ K) and magnetic-field strengths ($B < 10^{16}$ G) of interest, neutron stars consist of degenerate matter, typically characterized by temperatures lower than the Fermi temperature throughout their entire existence. In this specific temperature range, quantum effects, as dictated by Fermi statistics, overwhelmingly dominate over thermal effects. Therefore, the EOS for neutron stars can be effectively approximated as that of zero temperature, allowing us to largely ignore thermal contributions for most of their lifespan. In particular, here we present results of EOSs at zero temperature, describing both the star crust and the liquid core. This allows us to interpolate the provided tables using different schemes to obtain the relevant quantities, selected by the user. The EOS provides the input to compute at each point of the star the microphysics parameters, for example, $\eta(T)$, c_V , κ and Q_v , essential for our simulations. In particular, it is important to take into account superfluid and superconductive models for neutrons and protons, respectively, as they significantly impact the cooling timescales through their influence on c_V and Q_v . In addition, superfluidity and superconductivity activate an additional neutrino emission channel through ‘Cooper pair breaking and formation’ processes. This channel is triggered owing to the continuous formation and breaking of Cooper pairs. The effect of the superfluidity and superconductivity, namely, the suppression of specific heats, the creation of an additional neutrino channel and the suppression of neutrino emissivity, collectively influence the cooling process. While the suppression of neutrino emissivity slows down cooling, the other two effects accelerate it. Overall, unless extremely unusual choices are made for the gap models in the neutron star, cooling is typically accelerated. As the primary objective of this work is not to explore the vast parameter space encompassing superfluidity models, detailed discussions concerning their impact on cooling models and in particular on enhanced cooling are deferred to dedicated studies (for example, refs. 11,18,55–58). In this study, we utilize the superfluid gap proposed by ref. 59. Various additional microphysical ingredients play a crucial role in the interior of a neutron star. Notably, the EOS and superfluid models have a significant effect on the cooling process as already mentioned, but they play a comparatively smaller role in the evolution of the magnetic field, especially when compared with the initial topology chosen for the system.

For a comprehensive computation of the different microphysics ingredients (for example, neutrino emissivity, conductivities, magnetic diffusivity and so on) required for the heat diffusion equation and the induction equation in our simulations, we refer to the review by ref. 11 and exploring the publicly available codes developed by Alexander Potekhin (<http://www.ioffe.ru/astro/conduct/>). These resources offer valuable insights and tools for studying the intricate physics governing neutron stars.

To solve the induction equation (equation (1)), we consider the magnetic field confined in the crust of a neutron star assuming perfect conductor boundary condition at the crust/core interface and potential magnetic boundary conditions (current-free magnetosphere) at the outer numerical boundary, placed at density $\rho = 10^{10}$ g cm⁻³. Moreover, in this study, we focus solely on the axisymmetric evolution and do not consider the generalization to three dimensions, as performed in the recently developed MATINS code for coupled magneto-thermal evolution in isolated neutron stars^{60,61}.

We limit our analysis to solving the heat diffusion equation (assuming an initial temperature value of 10^{10} K) solely in the crust of the neutron star. This is owing to the fact that the core of a neutron star becomes isothermal a few decades after formation, due to its high

thermal conductivity. Meanwhile, the low-density region (envelope and atmosphere) quickly reaches radiative equilibrium, establishing a significant difference in thermal relaxation timescales compared with the interior (crust and core). This discrepancy makes it computationally expensive to perform cooling simulations on a numerical grid encompassing all layers up to the star's surface. Instead, for the outer layer, we rely on a separate calculation of stationary envelope models to derive a functional relationship between the surface temperature T_s (determining the radiation flux) and the temperature T_b at the crust/envelope boundary. This $T_s - T_b$ relation serves as the outer boundary condition for the heat transfer equation.

To account for surface radiation, we adopt a blackbody emission model. Given our focus on explaining the luminosity of faint and young objects, we specifically adopt the most updated iron envelope¹¹. Light-element envelope models, in contrast, result in approximately one order of magnitude brighter luminosity. For a more comprehensive examination of how envelope models with different compositions influence the cooling process, we direct the reader to ref. 30.

In this study, we use the latest version of the two-dimensional magneto-thermal code²⁴ to model nuclear matter. In addition, to model hyperon matter in the core of the star, we use the code in refs. 28,29, which is also based on ref. 24, but has been appropriately modified to calculate the magneto-thermal evolution in stars containing both nuclear and hyperon matter. This code smoothly matches the GM1A and GM1B EOSs²⁷ in the core with the SLy4 EOS²⁵ in the crust while also considering the influence of hyperon matter on the star's micro-physics. One crucial modification made in refs. 28,29, compared with ref. 24, is the superfluid gap model, which allows accurate descriptions of stars containing hyperons. Furthermore, the most significant effect of this study arises from the inclusion of the hyperon direct Urca channel and the Cooper pair of hyperons. These two neutrino cooling channels, especially the hyperon direct Urca one, lead to enhanced cooling in neutron stars at a young age.

Our simulations encompass various neutron-star background models, considering different masses $M = 1.4 M_\odot$, $1.6 M_\odot$ and $1.8 M_\odot$, along with diverse nuclear EOSs. We selected three EOSs for our investigation: BSK24²⁶, SLy4 Eos²⁵ and GM1A Eos²⁷ matched with the SLy4 EOS in the crust^{28,29}. Through magneto-thermal simulations, we observed distinctive cooling behaviours. Specifically, the SLy4 EOS²⁵ showed no activation of enhanced cooling. Conversely, the BSK24 EOS²⁶ showed enhanced cooling, triggered at a direct Urca threshold density of $8.25 \times 10^{14} \text{ g cm}^{-3}$. It is noteworthy that the latter EOS attains a maximum mass of $2.279 M_\odot$ and a corresponding central density of $2.26 \times 10^{15} \text{ g cm}^{-3}$. In the case of the GM1A EOS²⁷, our analysis revealed consistent activation of enhanced cooling across all examined masses, starting from a mass of $1.4 M_\odot$ and a density of $5.949 \times 10^{14} \text{ g cm}^{-3}$. This particular EOS reaches a maximum mass of $1.994 M_\odot$ and a corresponding central density of $2 \times 10^{15} \text{ g cm}^{-3}$.

Furthermore, we explore a wide range of initial magnetic-field values for the surface dipolar field, ranging from $1 \times 10^{12} \text{ G}$ to $7 \times 10^{13} \text{ G}$ at the pole. Our simulations are restricted to this range in accordance with our objective to analyse pulsars with magnetic fields ranging from 10^{12} G to a few 10^{13} G , as confirmed by observational measurements. To maintain focus on the cold-neutron-star scenario, we intentionally excluded the inclusion of a toroidal field in our simulations. This decision was made to prevent Joule heating and to avoid scenarios where the dissipation of the magnetic field in the highly resistive crust might obscure the effects of enhanced cooling mechanisms in stars with magnetic fields exceeding 10^{14} G (ref. 18). In Supplementary Fig. 2, we show the same simulations as for Fig. 1 but showing the period and period derivative evolution.

On the effect of choosing different envelopes

In this section, we explain the reasoning behind some of the assumptions and/or simplifications we make in this study, in particular

concerning the neutron-star envelope, and the ages and distances we use for the three cold neutron stars we present.

Neutron-star envelopes might be composed by a variety of elements, from the lightest ones such as hydrogen or helium, to heavy envelopes such as iron. The envelope composition might differ from source to source depending on its exact evolutionary history, and they are known to show different cooling evolution³⁰. Cooling simulations by many authors show how heavy envelopes systematically result in cooler temperatures at younger ages. We have chosen to use here only the simulations using the heavy envelope as we aimed at the modelling of very faint sources; hence, we assumed the most extreme case. If these objects would possess a light envelope, the need of enhanced cooling would be even more pronounced.

However, although initially considering also the pulsar PSR B0656+14 among the extremely cold sources, while performing simulations using also light envelopes³⁰, we saw that at such older ages ($>10^4 \text{ yr}$), the cooling curves might behave differently (Extended Data Fig. 4). In particular, using light envelopes, even EOSs not activating enhanced-cooling processes might explain this object.

In Extended Data Fig. 4, we also show simulations for a $2 M_\odot$ source, showing how even for this extreme mass the SLy4 does not activate any enhanced-cooling mechanism.

Statistical analysis

To constrain the nature of each source, we start comparing their observed parameters, L_{th} , P and \dot{P} , against the tracks of the 81 simulations in the same 3D parameter space (Extended Data Fig. 5), each containing 128 points corresponding to various times from the formation of the neutron star up to ~100 kyr age (0, 1.3, 1.5, 1.8, ..., 81,200, 97,400 yr). Ideally, the most probable parameters (EOS, mass and B_p) of a given source are those of the simulated neutron star sharing the same observed features. However, owing to the finiteness of the simulations, and the uncertainty on the luminosity (we ignore the uncertainties on P and \dot{P} as the relative uncertainty on L_{th} is significantly higher), there is no simulation passing exactly through the positions of the sources in the feature space. In addition, multiple simulations may be found in the vicinity of the sources (Extended Data Fig. 5). Consequently, we opt for a machine learning model that given the observational and simulation data, can identify the most probable simulations, and as a consequence, the posterior distribution of the parameters, namely, the EOS, mass and B_p . We tried with two approaches, deep learning and classification, explained in detail in the next sections.

The deep learning approach

The simulation parameters are either categorical (EOS) or continuous (mass and B_p). If the categorical and continuous parameters could be constrained by mutually exclusive sets of features (for example, if the EOS could be constrained only by L_{th} , while mass and B_p , only by P and \dot{P}), then their estimation could rely on independent classification and regression models on the independent sets of inputs and outputs. However, this is not the case in the simulations: we need to employ a machine learning approach that performs both classification and regression simultaneously. We used a neural network that learns the parameters (EOS, mass and B_p) given a specific point in the feature space (L_x , P and \dot{P}), trained on the simulation data. Specifically, using TENSORFLOW⁶², we constructed a multilayer perceptron neural network that predicts the parameters, with a loss function being the sum of the loss for the EOS, and the loss for the values of mass and B_p . The architecture is summarized as an input layer of size 3 (for the 3 features), fully connected hidden layers (with rectified linear unit activation functions) and 2 output layers connected to the last hidden layer: (1) the classification output layer of size 3 and softmax activation function (for the classification probabilities for BSK24, SLy4, SLy4 + GM1A), and the (2) regression output layer of size 2 and linear activation function (for the mass and B_p). We tried different numbers and sizes of

hidden layers, loss functions (for example, mean squared error of the regression output, and cross entropy for the classification output). We found that the models were converging slowly (up to 10,000 epochs) with poor results: the best accuracy in predicting the EOS class was ~65%, which is not significant with respect to a dummy classifier (33% accuracy if randomly assigning one of the three EOSs) and the classification approach below (90% accuracy). Increasing the number of simulations would aid the neural network in learning the feature space; however, owing to their computational complexity, we employed the classification approach.

The classification approach

Interestingly, classification can be seen as ‘discretized’ regression: instead of estimating the mass of a neutron star, we can classify it into distinct mass classes, $1.4 M_{\odot}$, $1.6 M_{\odot}$ and $1.8 M_{\odot}$. However, training three classifiers for EOS, mass and B_p is not optimal as this ignores the interplay between the parameters in the evolution of neutron stars imprinted in the feature space. In our case, each simulation corresponds to a combination of EOS, mass and B_p classes, and, therefore, there is only one class: the simulation class, which can be modelled as the ID of the simulation (that is, k corresponding to the k th simulation). This is a simple classification task that can be easily carried out with standard, well-understood machine learning classifiers that are easily trained on small datasets. Using a probabilistic classification algorithm to predict the simulation class, we can predict the classification probability of each simulation for each observed source. Then, the posterior of each parameter to have a specific value is simply the sum of all the classification probabilities of the simulations sharing the same value. For example, the posterior of the EOS of a source being BSK24 is the sum of the classification probabilities of all the simulations (classes) for which the EOS is BSK24, predicted on the features of the source:

$$P(\text{BSK24}) = \sum_{k=1}^n P(\text{BSK24} = \text{EOS}_k) \pi_k \quad (3)$$

where $P(\text{BSK24} = \text{EOS}_k)$ is either 1 or 0, denoting whether the BSK24 EOS was used in the k th simulation, π_k is the prior on the class which in our case is the classification probability of the k th simulation when predicting the class of the observation, and n is the total number of simulations. The same approach is used for the continuous parameters as well (mass and B_p), with the output being still the marginal probabilities at the distinct values used in the simulations.

We stress that one should be careful in the interpretation of the various classification metrics (for example, accuracy). The number of simulation classes depends on the choices for the range and resolution in the initial conditions, which are generally restricted due to technical and modelling difficulties (for example, computational cost, available EOS models and so on). Ideally, a large number of simulations could be run, leading to a paradox: due to the continuous nature of the mass and B_p , the classification probability would approach zero even if the ‘correct’ model is present in the training. Consequently, the absolute scale of the accuracy of the trained classifier is not an estimate of the performance of the methodology. Conversely, the relative accuracy between different algorithms (or hyperparameters) measures their relative ability to learn the feature space given the simulation choices and the observational uncertainties.

Selection of classifier and hyperparameters

To select the classification algorithm, we design a cross-validation test bed. We consider eight different classifiers offered by the SCIKIT-LEARN package⁶³: k -nearest neighbour, random forest, decision tree, logistic, support vector, nu-support vector, multilayer perceptron and Gaussian process classifier, and multiple hyperparameter choices for each (three to ten different values for a key hyperparameter such as k for the k -nearest neighbour, or the kernel for the Gaussian process classifier).

We set aside one-sixth of the data as a test dataset that will be used to estimate the accuracy of the classifier with the best hyperparameters. The remaining dataset is separated in five folds of equal fractions (one-sixth of the original data). A fivefold cross-validation approach is adopted to measure the accuracy of the different classifiers and hyperparameter choices. However, the test samples fall very close to the training samples as they follow distinct curves in the feature space. Consequently, most classifiers will show very high performance, which does not reflect the accuracy when applied in real data, which are subject to measurement uncertainties. For this reason, we ‘disturb’ the cross-validation samples by adding Gaussian noise in the decimal logarithm of the luminosity of the simulations (we ignore the uncertainties on P and P as they are negligible), to simulate the presence of uncertainty. We train, cross-validate and test the classifiers at 6 different scales for the uncertainty: 0 (no disturbance), 0.05, 0.10, 0.15, 0.2, 0.25 and 0.30 dex, a range that includes the uncertainty on L_{th} in our sources (close to 0.2 dex).

For each classifier and L_{th} uncertainty level, we use the cross-validation technique to optimize for the hyperparameters. Then, using the test dataset, we measure the accuracy score, that is, the fraction of test data points that the algorithm was able to match to their original track. Trying all classification algorithms initially, we found that the k -nearest-neighbour and random-forest classifiers showed the highest accuracy scores. In addition, they are computationally efficient during both training and prediction. For this reason, we focus on these two classification methods from now on. In the top left panel of Supplementary Fig. 3, with solid lines, we show the accuracy of the k -nearest-neighbour and the random-forest classifiers, as a function of the L_{th} uncertainty level. Both algorithms perform equally well. For the prediction of the properties of the observed source, we select the random-forest classifier because it performs better at high uncertainties (≥ 0.2 dex). In addition, the random-forest classifier has two attractive properties: it is not sensitive to the scale of the features and it is intrinsically a probabilistic algorithm.

Finally, as we are interested in the ability to predict the physical properties of the pulsars, we measure the marginal accuracy of the classifiers, that is, the ability to predict them independently. For example, if a test data point corresponds to a model with $M = 1.4 M_{\odot}$, does the predicted model have the same mass (no matter what the EOS or B_p)? In the top right, bottom left and bottom right panels of Supplementary Fig. 3, we show the marginalized accuracy for the EOS, mass and B_p , respectively (with solid lines). We find that the magnetic field is easier to be learned (>95% accuracy), while the EOS and mass are sometimes mismatched (43–95% accuracy), especially at high uncertainty levels. The fact that the accuracy score is not 100% even with no added noise in the luminosity reflects the degeneracy between the models: as can be seen in Extended Data Fig. 5, the tracks of the different simulations often occupy the same regions of the feature space. Here we remind that the accuracy score should be used only for comparisons of algorithms, and not as a measure of performance of the methodology.

Predictions accounting for the uncertainty on the luminosity

We use the random-forest classifier that has been optimized for the level of L_{th} uncertainty in our observations, retrained using all the available simulation data (without separation to training, validation and test datasets⁶⁴). However, the uncertainty of the luminosity is not used directly during prediction. To take into account the observational uncertainty of a given source’s luminosity, we use a Monte Carlo approach: we sample the error distribution of the luminosity 100,000 times, predict the properties of the sources and sum the results. To sample the error distribution of the luminosity, we use Monte Carlo uncertainty propagation: we model the error distributions of the flux and the distance, draw samples from them and calculate the luminosity samples. This is to avoid standard uncertainty propagation for three reasons: (1) we have high relative uncertainties in the quantities

involved; (2) the flux and distance confidence intervals are not symmetric (especially in the case of the distance of PSR B2334+61); (3) the classifier operates in log-space where even symmetric error bars are transformed into asymmetric ones. We note that applying the standard uncertainty propagation formula by averaging the low and high error bars resulted in ~20% differences in the resulting classification probabilities with respect to the Monte Carlo uncertainty propagation using asymmetric error distributions as outlined below.

First, we represent the flux and distance uncertainties using the binormal distribution, which is flexible enough to represent asymmetric distributions. A binormal distribution's probability density function is the result of stitching together the opposite halves of two distinct normal distributions with the same mean value (which acts as the mode of the new distribution) but different standard deviations⁶⁵. Consequently, we represent each flux and distance measurement with a binormal distribution by adopting the measured value as the mode, and fitting for the two standard deviations such that the reported confidence intervals are matching those of the binormal distribution. In Supplementary Fig. 4, we show the probability density functions of the constructed binormal distributions (in the form of histograms of their samples) for the flux and distance (left and middle panels, respectively) of the two sources for which we apply the classification, as well as the derived luminosity error distribution.

We predict the probability of the 81 simulations, 100,000 times (for each sample from the L_{th} distribution) for each source. By summing up the 100,000 results, we find the classification probability for each model. In the top panel of Supplementary Table 2, we show the models with the highest classification probabilities, and in Fig. 2 we visualize all the results. In addition, in Supplementary Table 2, we report the marginalized probability for the EOS, mass and B_p of each source, which are also shown in Supplementary Fig. 5.

Accounting for the age information

As the simulations track the evolution of the properties of the pulsars in time, if the real age of the source is known, it provides an additional constraint. We add the time as another input variable, making the feature space 4D, and then repeat the above analysis: (1) optimize the two classification algorithms for different luminosity uncertainty scales (see dotted lines in Supplementary Fig. 3); (2) select the random-forest classifier optimized for the 0.2 dex uncertainty scale (it outperforms the k -nearest-neighbour classifier at uncertainty scales >0.1 dex); (3) predict the parameters of the two sources using the age estimates in Extended Data Table 1.

Having a 4D feature space, it is impossible to visually inspect its coverage by the simulation tracks. Instead, we ensured that the observed sources fall within the range of the simulation evolutionary tracks by confirming that their positions are inside a simplex of the Delaunay hypertetrahedralization of the simulation data.

The predictions of the 4D classifier are shown in Extended Data Table 5 and Supplementary Fig. 5 (with red rectangles). These results are for the most part consistent with the 3D classifier. For both sources, the 3D and 4D classifiers indicate the same most probable value for B_p . For PSR J0205+6449, the most probable values for the EOS and mass are the same, while for PSR J0205+6449 they differ, but not significantly (BSK24 and GMIA EOS, and $1.6 M_{\odot}$ and $1.8 M_{\odot}$ masses have high marginal posteriors >25%).

We notice that the posteriors in the 4D case are less ‘peaky’. This is in contrast to our expectation that adding another feature (age) would create larger contrast between the marginal probabilities (effectively lowering the entropy of information). Given the small number of EOSs in our simulations, at this stage, we do not consider our method well suited to constrain the EOS itself. Nevertheless, for both sources, our statistical analysis does show that the SLy4 EoS and the $1.4 M_{\odot}$ mass scenario are found to be highly improbable with or without considering the age information.

Data availability

The data that support this paper are publicly available in the XMM-Newton and Chandra archives. Further data products can be supplied by the corresponding authors on request.

Code availability

The codes that support this paper are available upon request to the corresponding authors.

References

1. Baym, G., Pethick, C. & Sutherland, P. The ground state of matter at high densities: equation of state and stellar models. *Astrophys. J.* **170**, 299 (1971).
2. Pacini, F. Energy emission from a neutron star. *Nature* **216**, 567–568 (1967).
3. Harding, A. K. & Lai, D. Physics of strongly magnetized neutron stars. *Rep. Prog. Phys.* **69**, 2631–2708 (2006).
4. Prakash, M. et al. Composition and structure of protoneutron stars. *Phys. Rep.* **280**, 1–77 (1997).
5. Page, D., Lattimer, J. M., Prakash, M. & Steiner, A. W. Minimal cooling of neutron stars: a new paradigm. *Astrophys. J. Suppl. Ser.* **155**, 623–650 (2004).
6. Flowers, E., Ruderman, M. & Sutherland, P. Neutrino pair emission from finite-temperature neutron superfluid and the cooling of young neutron stars. *Astrophys. J.* **205**, 541–544 (1976).
7. Prakash, M., Prakash, M., Lattimer, J. M. & Pethick, C. J. Rapid cooling of neutron stars by hyperons and delta isobars. *Astrophys. J. Lett.* **390**, L77 (1992).
8. Prakash, M. & Lattimer, J. M. Strangeness in stellar matter. *Nat. Phys.* **639**, 433–442 (1998).
9. Ho, W. C. G. & Heinke, C. O. A neutron star with a carbon atmosphere in the Cassiopeia A supernova remnant. *Nature* **462**, 71–73 (2009).
10. Beznogov, M. V. & Yakovlev, D. G. Statistical theory of thermal evolution of neutron stars—II. Limitations on direct Urca threshold. *Mon. Not. R. Astron. Soc.* **452**, 540–548 (2015).
11. Potekhin, A. Y., Pons, J. A. & Page, D. Neutron stars—cooling and transport. *Space Sci. Rev.* **191**, 239–291 (2015).
12. Potekhin, A. Y. & Chabrier, G. Magnetic neutron star cooling and microphysics. *Astron. Astrophys.* **609**, A74 (2018).
13. Jonker, P. G., Bassa, C. G. & Wachter, S. The quasi-persistent neutron star soft X-ray transient 1M 1716–315 in quiescence. *Mon. Not. R. Astron. Soc.* **377**, 1295–1300 (2007).
14. Heinke, C. O., Jonker, P. G., Wijnands, R. & Taam, R. E. Constraints on thermal X-ray radiation from SAX J1808.4–3658 and implications for neutron star neutrino emission. *Astrophys. J.* **660**, 1424–1427 (2007).
15. Brown, E. F. et al. Rapid neutrino cooling in the neutron star MXB 1659–29. *Phys. Rev. Lett.* **120**, 182701 (2018).
16. Mendes, M., Fattoev, F. J., Cumming, A. & Gale, C. Fast neutrino cooling in the accreting neutron star MXB 1659–29. *Astrophys. J.* **938**, 119 (2022).
17. Potekhin, A. Y., Gusakov, M. E. & Chugunov, A. I. Thermal evolution of neutron stars in soft X-ray transients with thermodynamically consistent models of the accreted crust. *Mon. Not. R. Astron. Soc.* **522**, 4830–4840 (2023).
18. Aguilera, D. N., Pons, J. A. & Miralles, J. A. 2D cooling of magnetized neutron stars. *Astron. Astrophys.* **486**, 255–271 (2008).
19. Kothes, R. Distance and age of the pulsar wind nebula 3C 58. *Astron. Astrophys.* **560**, A18 (2013).
20. Yar-Uyaniker, A., Uyaniker, B. & Kothes, R. Distance of three supernova remnants from H I line observations in a complex region: G114.3+0.3, G116.5+1.1, and CTB 1 (G116.9+0.2). *Astrophys. J.* **616**, 247–256 (2004).

21. Allen, G. E. et al. On the expansion rate, age, and distance of the supernova remnant G266.2–1.2 (Vela Jr.). *Astrophys. J.* **798**, 82 (2015).
22. Pons, J. A., Miralles, J. A. & Geppert, U. Magneto-thermal evolution of neutron stars. *Astron. Astrophys.* **496**, 207–216 (2009).
23. Viganò, D. et al. Unifying the observational diversity of isolated neutron stars via magneto-thermal evolution models. *Mon. Not. R. Astron. Soc.* **434**, 123–141 (2013).
24. Viganò, D., Garcia-Garcia, A., Pons, J. A., Dehman, C. & Graber, V. Magneto-thermal evolution of neutron stars with coupled ohmic, Hall and ambipolar effects via accurate finite-volume simulations. *Comput. Phys. Commun.* **265**, 108001 (2021).
25. Douchin, F. & Haensel, P. A unified equation of state of dense matter and neutron star structure. *Astron. Astrophys.* **380**, 151–167 (2001).
26. Pearson, J. M. et al. Unified equations of state for cold non-accreting neutron stars with Brussels–Montreal functionals - I. Role of symmetry energy. *Mon. Not. R. Astron. Soc.* **481**, 2994–3026 (2018).
27. Gusakov, M. E., Haensel, P. & Kantor, E. M. Physics input for modelling superfluid neutron stars with hyperon cores. *Mon. Not. R. Astron. Soc.* **439**, 318–333 (2014).
28. Anzuini, F., Melatos, A., Dehman, C., Viganò, D. & Pons, J. A. Fast cooling and internal heating in hyperon stars. *Mon. Not. R. Astron. Soc.* **509**, 2609–2623 (2021).
29. Anzuini, F., Melatos, A., Dehman, C., Viganò, D. & Pons, J. A. Thermal luminosity degeneracy of magnetized neutron stars with and without hyperon cores. *Mon. Not. R. Astron. Soc.* **515**, 3014–3027 (2022).
30. Dehman, C., Pons, J. A., Viganò, D. & Rea, N. How bright can old magnetars be? Assessing the impact of magnetized envelopes and field topology on neutron star cooling. *Mon. Not. R. Astron. Soc.* **520**, L42–L47 (2023).
31. Margueron, J., Hoffmann Casali, R. & Gulminelli, F. Equation of state for dense nucleonic matter from metamodeling. II. Predictions for neutron star properties. *Phys. Rev. C* **97**, 025806 (2018).
32. Kuiper, L. et al. Hard X-ray timing and spectral characteristics of the energetic pulsar PSR J0205+6449 in supernova remnant 3C 58. An RXTE PCA/HEXTE and XMM-Newton view on the 0.5–250 keV band. *Astron. Astrophys.* **515**, A34 (2010).
33. Abdo, A. A. et al. Discovery of pulsations from the pulsar J0205+6449 in SNR 3C 58 with the Fermi Gamma-Ray Space Telescope. *Astrophys. J. Lett.* **699**, L102–L107 (2009).
34. Furst, E., Reich, W. & Seiradakis, J. H. A new pulsar-supernova remnant association: PSR 2334+61 and G 114.3+0.3. *Astron. Astrophys.* **276**, 470–472 (1993).
35. Camilloni, F. et al. SRG/eROSITA and XMM-Newton observations of Vela Jr. *Astron. Astrophys.* **673**, A45 (2023).
36. Aschenbach, B. Discovery of a young nearby supernova remnant. *Nature* **396**, 141–142 (1998).
37. Kargaltsev, O., Pavlov, G. G., Sanwal, D. & Garmire, G. P. The compact central object in the supernova remnant G266.2–1.2. *Astrophys. J.* **580**, 1060–1064 (2002).
38. Mignani, R. P. et al. The nature of the infrared counterpart and of the optical nebula associated with the central compact object in Vela Jr. *Mon. Not. R. Astron. Soc.* **486**, 5716–5725 (2019).
39. Bietenholz, M. F. Radio Images of 3C 58: expansion and motion of its wisp. *Astrophys. J.* **645**, 1180–1187 (2006).
40. Roberts, D. A., Goss, W. M., Kalberla, P. M. W., Herbstmeier, U. & Schwarz, U. J. High resolution HI observations of 3C 58. *Astron. Astrophys.* **274**, 427–438 (1993).
41. Ranasinghe, S. & Leahy, D. Distances, radial distribution, and total number of galactic supernova remnants. *Astrophys. J.* **940**, 63 (2022).
42. Bietenholz, M. F. et al. The proper motion of PSR J0205+6449 in 3C 58. *Mon. Not. R. Astron. Soc.* **431**, 2590–2598 (2013).
43. Cordes, J. M. & Lazio, T. J. W. NE2001.I. A new model for the galactic distribution of free electrons and its fluctuations. Preprint at <https://arxiv.org/abs/astro-ph/0207156> 2002).
44. McGowan, K. E., Zane, S., Cropper, M., Vestrand, W. T. & Ho, C. Evidence for surface cooling emission in the XMM-Newton spectrum of the X-Ray pulsar PSR B2334+61. *Astrophys. J.* **639**, 377–381 (2006).
45. Slane, P., Helfand, D. J., van der Swaluw, E. & Murray, S. S. New constraints on the structure and evolution of the pulsar wind nebula 3C 58. *Astrophys. J.* **616**, 403–413 (2004).
46. Strüder, L. et al. The European Photon Imaging Camera on XMM-Newton: the pn-CCD camera. *Astron. Astrophys.* **365**, L18–L26 (2001).
47. Verner, D. A., Ferland, G. J., Korista, K. T. & Yakovlev, D. G. Atomic data for astrophysics. II. New analytic FITS for photoionization cross sections of atoms and ions. *Astrophys. J.* **465**, 487 (1996).
48. Wilms, J., Allen, A. & McCray, R. On the absorption of X-rays in the interstellar medium. *Astrophys. J.* **542**, 914–924 (2000).
49. Anders, E. & Grevesse, N. Abundances of the elements—meteoritic and solar. *Geochim. Cosmochim. Acta* **53**, 197–214 (1989).
50. Goodman, J. & Weare, J. Ensemble samplers with affine invariance. *Commun. Appl. Comput. Sci.* **5**, 65–80 (2010).
51. Heinke, C. O. et al. Discovery of a second transient low-mass X-ray binary in the globular cluster NGC 6440. *Astrophys. J.* **714**, 894–903 (2010).
52. Özel, F. & Freire, P. Masses, radii, and the equation of state of neutron stars. *Annu. Rev. Astron. Astrophys.* **54**, 401–440 (2016).
53. Pons, J. A. & Viganò, D. Magnetic, thermal and rotational evolution of isolated neutron stars. *Living Rev. Comput. Astrophys.* **5**, 3 (2019).
54. Pons, J. A., Viganò, D. & Rea, N. A highly resistive layer within the crust of X-ray pulsars limits their spin periods. *Nat. Phys.* **9**, 431–434 (2013).
55. Yakovlev, D. G., Levenfish, K. P. & Shibakov, Y. A. Cooling of neutron stars and superfluidity in their cores. *Phys. Uspekhi* **42**, 737–778 (1999).
56. Yakovlev, D. G., Kaminker, A. D., Gnedin, O. Y. & Haensel, P. Neutrino emission from neutron stars. *Phys. Rept.* **354**, 1 (2001).
57. Page, D., Geppert, U. & Weber, F. The cooling of compact stars. *Nucl. Phys. A* **777**, 497–530 (2006).
58. Page, D., Lattimer, J. M., Prakash, M. & Steiner, A. W. Neutrino emission from cooper pairs and minimal cooling of neutron stars. *Astrophys. J.* **707**, 1131–1140 (2009).
59. Ho, W. C., Elshamouty, K. G., Heinke, C. O. & Potekhin, A. Y. Tests of the nuclear equation of state and superfluid and superconducting gaps using the cassiopeia a neutron star. *Phys. Rev. C* **91**, 015806 (2015).
60. Dehman, C., Viganò, D., Pons, J. A. & Rea, N. 3D code for MAGneto-Termal evolution in Isolated Neutron Stars, MATINS: the magnetic field formalism. *Mon. Not. R. Astron. Soc.* **518**, 1222–1242 (2023).
61. Dehman, C., Viganò, D., Ascenzi, S., Pons, J. A. & Rea, N. 3D evolution of neutron star magnetic fields from a realistic core-collapse turbulent topology. *Mon. Not. R. Astron. Soc.* **523**, 5198–5206 (2023).
62. Abadi, M. et al. TensorFlow: large-scale machine learning on heterogeneous systems (TensorFlow, 2015); <https://www.tensorflow.org/>
63. Pedregosa, F. et al. Scikit-learn: machine learning in Python. *J. Mach. Learn. Res.* **12**, 2825–2830 (2011).
64. Tsamardinos, I. Don't lose samples to estimation. *Patterns* **3**, 100612 (2022).
65. Wallis, K. F. The two-piece normal, binormal, or double Gaussian distribution: its origin and rediscoveries. *Stat. Sci.* **29**, 106–112 (2014).

66. Murray, S. S., Slane, P. O., Seward, F. D., Ransom, S. M. & Gaensler, B. M. Discovery of X-ray pulsations from the compact central source in the supernova remnant 3C 58. *Astrophys. J.* **568**, 226–231 (2002).
67. Dewey, R. J., Taylor, J. H., Weisberg, J. M. & Stokes, G. H. A search for low-luminosity pulsars. *Astrophys. J. Lett.* **294**, L25–L29 (1985).
68. Dewey, R. J., Taylor, J. H., Maguire, C. M. & Stokes, G. H. Period derivatives and improved parameters for 66 pulsars. *Astrophys. J.* **332**, 762 (1988).

Acknowledgements

A.M., C.D. and N.R. are supported by the ERC Consolidator Grant 'MAGNESIA' number 817661 (principal investigator N.R.) and SGR2021.01269 funded by the Generalitat de Catalunya (principal investigators V. Gruber and N.R.). C.D. acknowledges the doctoral programme in Physics of the Universitat Autònoma de Barcelona and the Nordita Visiting PhD Fellow programme. K.K. is supported by a fellowship programme at the Institute of Space Sciences (ICE-CSIC) funded by the programme Unidad de Excelencia María de Maeztu CEX2020-001058-M. J.A.P. acknowledges support from the Generalitat Valenciana grants ASFAE/2022/026 (with funding from NextGenerationEU PRTR-C17.I1) and CIPROM/2022/13, and from the AEI grant PID2021-127495NB-I00 funded by MCIN/AEI/10.13039/501100011033 and by 'ESF Investing in your future'. D.V. is supported by the ERC Starting Grant 'IMAGINE' number 948582 (principal investigator D.V.). K.K. thanks the 'Summer School for Astrostatistics in Crete' for providing training on the statistical methods adopted in this work. We thank F. Anzuini for providing his hyperon EOS implementation and for detailed comments on the paper as well as L. Tolos, C. Manuel, D. De Grandis, S. Ascenzi, V. Gruber, F. Gulminelli, M. Oertel, A. Borghese and F. Coti Zelati for feedback and comments.

Author contributions

The project was conceived, planned and organized by N.R., who wrote the final paper. The three main parts of the work were performed by A.M., C.D. and K.K., namely, the observational data analysis, the

magneto-thermal simulations and the machine learning statistical analysis, respectively. They were also in charge of writing the relative sections in Methods. J.A.P., D.V. and C.D. wrote the magneto-thermal simulation code used in this work. All authors discussed and commented on the final complete paper.

Competing interests

The authors declare no competing interests.

Additional information

Extended data is available for this paper at <https://doi.org/10.1038/s41550-024-02291-y>.

Supplementary information The online version contains supplementary material available at <https://doi.org/10.1038/s41550-024-02291-y>.

Correspondence and requests for materials should be addressed to A. Marino, C. Dehman, K. Kovlakas or N. Rea.

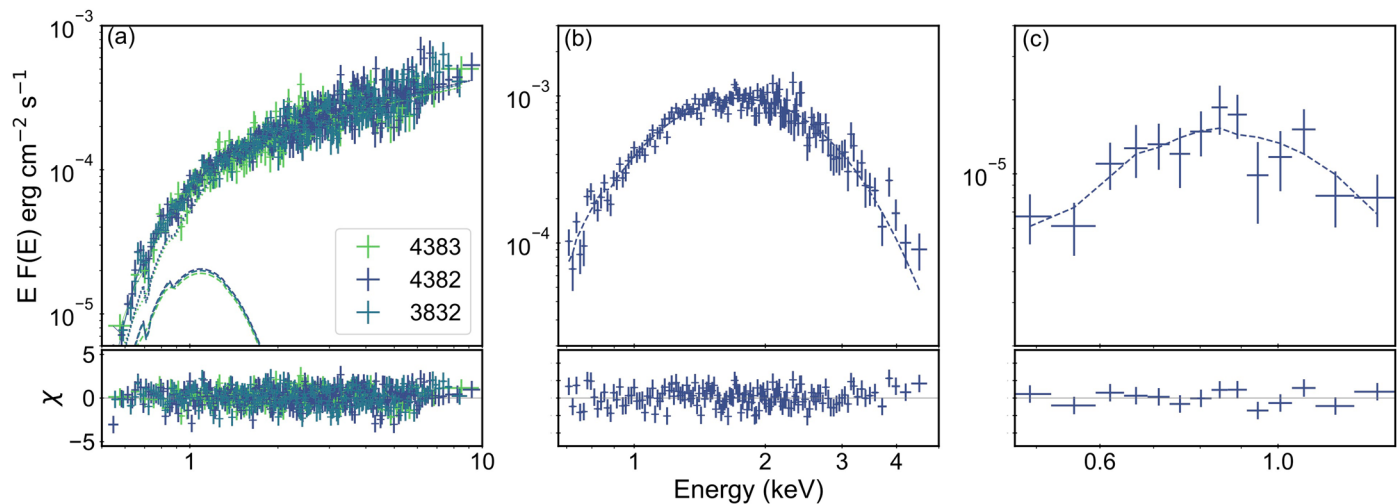
Peer review information *Nature Astronomy* thanks Nathalie Degenaar, Andrew Steiner and Lami Suleiman for their contribution to the peer review of this work.

Reprints and permissions information is available at www.nature.com/reprints.

Publisher's note Springer Nature remains neutral with regard to jurisdictional claims in published maps and institutional affiliations.

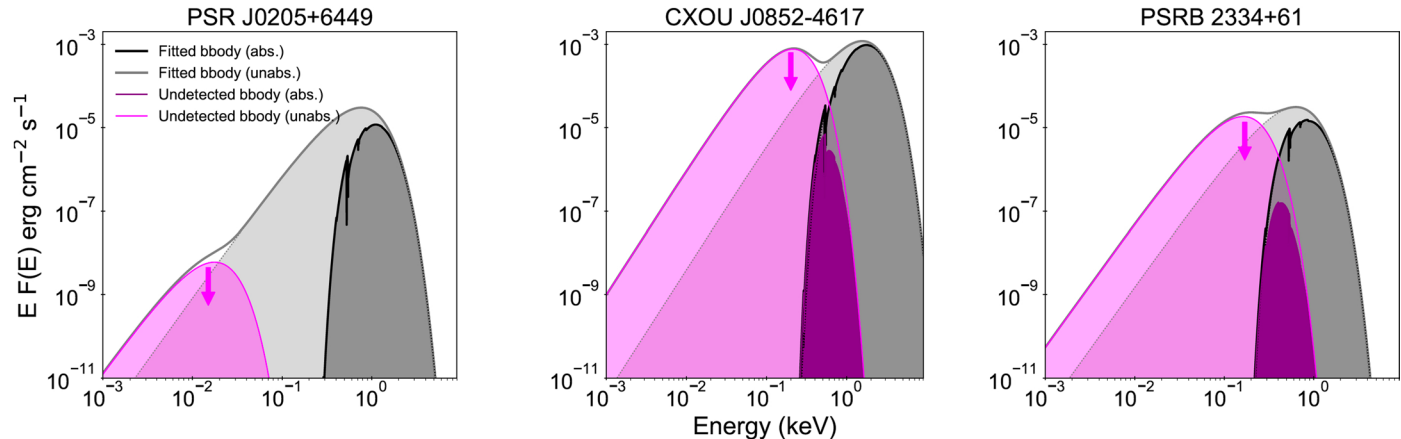
Springer Nature or its licensor (e.g. a society or other partner) holds exclusive rights to this article under a publishing agreement with the author(s) or other rightsholder(s); author self-archiving of the accepted manuscript version of this article is solely governed by the terms of such publishing agreement and applicable law.

© The Author(s), under exclusive licence to Springer Nature Limited 2024



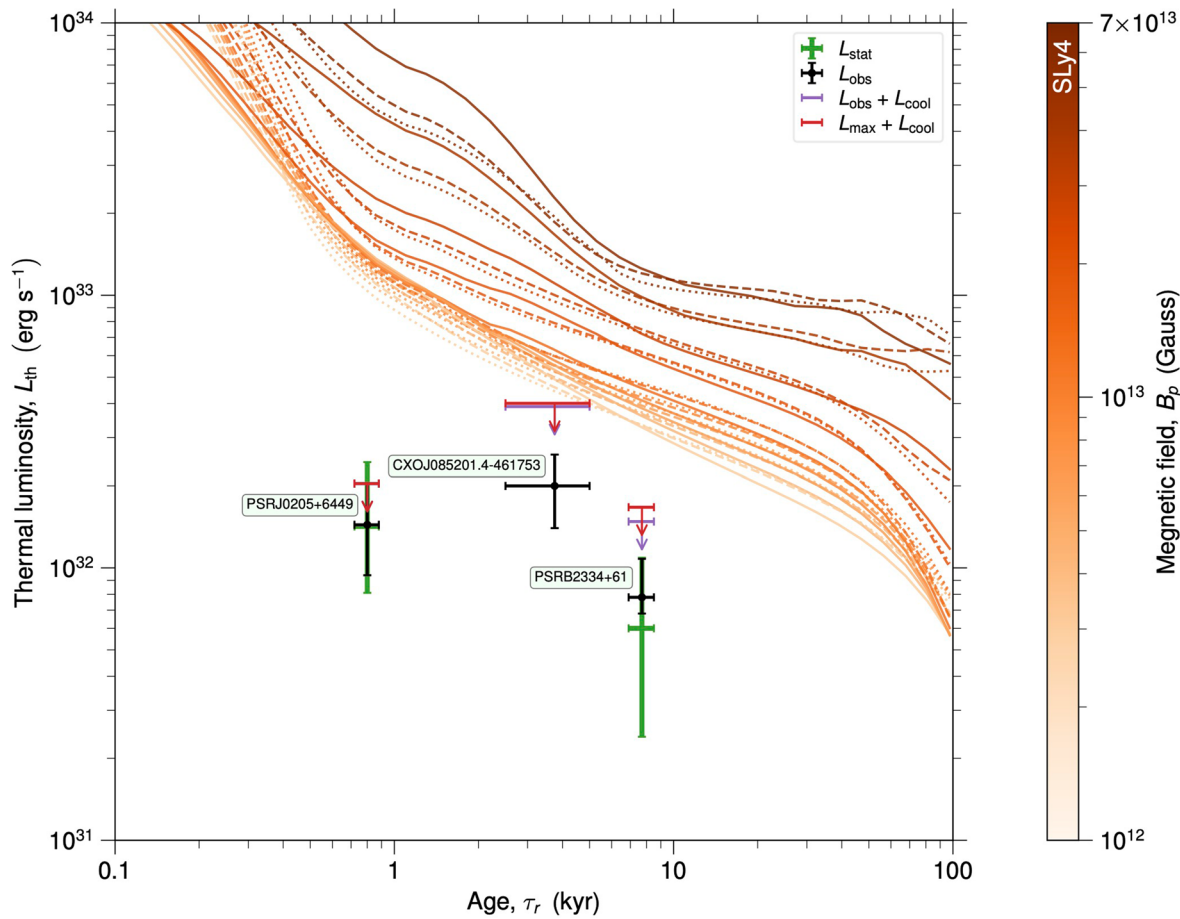
Extended Data Fig. 1 | Energy Spectra. Best-fit model and residuals for the three sources used in this manuscript, that is, (a): PSR J0205+6449 (using three different observations labelled with the relative ID; see Extended Data Table 3),

(b): PSR B2334+61, (c): CXOU J0852-4617. Different line styles were adopted to distinguish between the different components, that is dotted for POWERLAW and dashed for BBODYRAD.



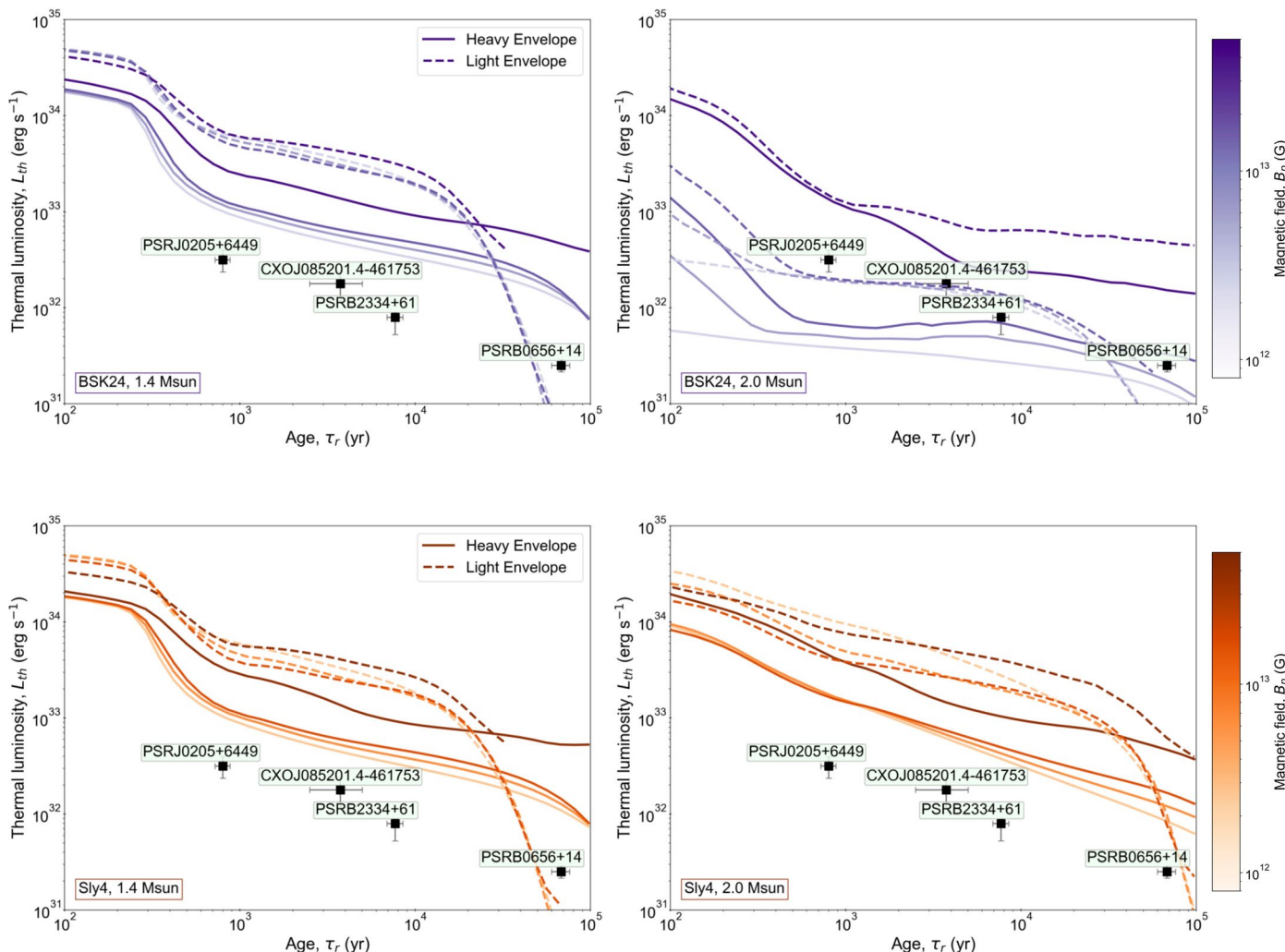
Extended Data Fig. 2 | Thermal luminosity components. Comparison between best-fit models of the thermal emission in the three sources used in this work and the cold, undetected blackbody components which may possibly be emitted by the whole NS surface but hidden out by interstellar absorption (see Extended

Data Table 2 for the exact values and errors). The absorbed components are displayed with bolder lines and colors to distinguish them from the unabsorbed components.



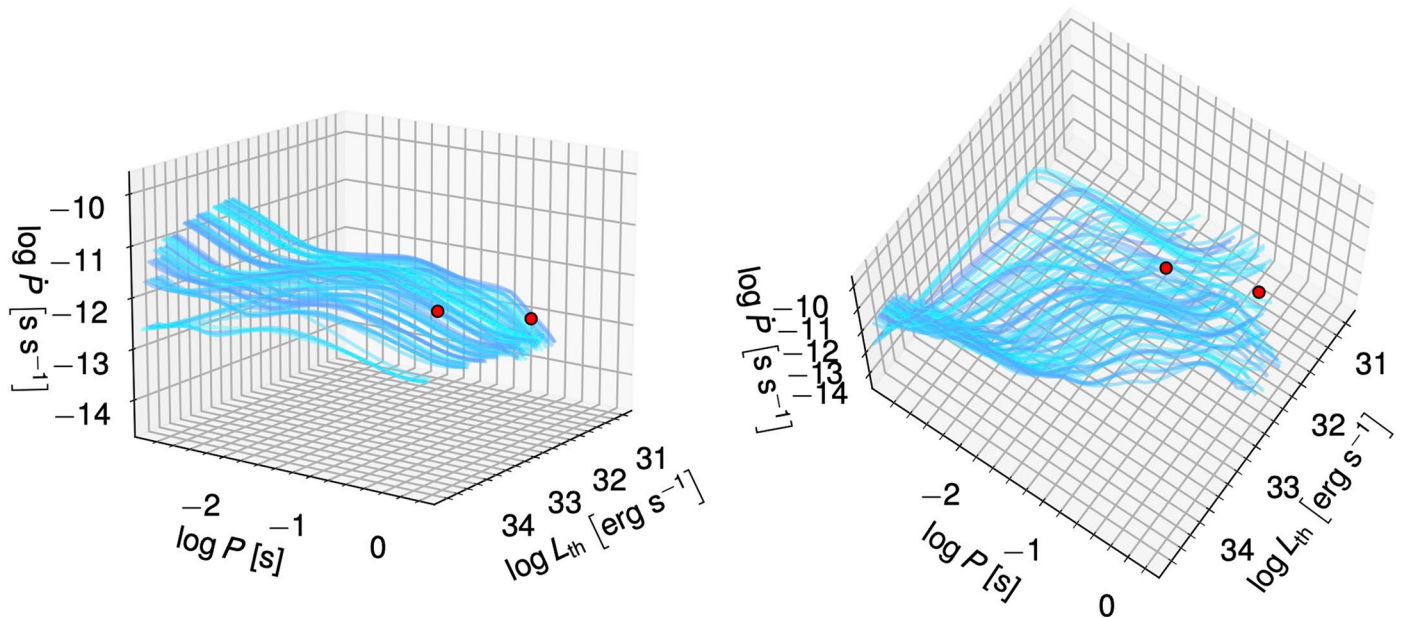
Extended Data Fig. 3 | Comparison between luminosities. We plot here all the luminosities obtained in this work (see Supplementary Table 1) and theoretical cooling curves simulated adopting SLy4 as EoS. The curves are stylised following the same prescriptions as in Fig. 1. For each of the three sources we show L_{obs} (L_{stat}) with black (green) error bars. Upper limits on the luminosity of each sources,

calculated as $L_{\text{obs}} + \Delta L_{\text{obs}} + L_{\text{cool}}$ (with ΔL_{obs} the 1- σ error on L_{obs}), are displayed with purple vertical arrows. An alternative version of the upper limits, using the highest flux from all models (three atmosphere models and the adopted blackbody model are shown with red vertical arrows; see Extended Data Tables 3–4 for the exact values and error determinations).



Extended Data Fig. 4 | Comparison between cooling tracks with different envelopes. We produced cooling curves using heavy (solid lines) and light (dashed lines) envelopes. The curves in the top (bottom) panels were produced using BSK24 (Sly4) and are coloured with purple (orange). Different shades of

the same colours are used to identify different values of the magnetic fields, as shown in the colour bars. The observed values of PSRJ0205+6449, PSR B2334+61, CXOUJ0852-4617 and PSR B0656+14 are reported in each panel. Errors in the luminosities are calculated as described in the Methods section.



Extended Data Fig. 5 | Period-Period Derivative-Luminosity tracks. The tracks of our 3D simulations in the $P - \dot{P} - L_{\text{th}}$ space in a time span of 100 kyr (cyan lines) from two different view angles (left and right panels). The positions of PSR J0205+6449 and PSR B2334+61 are denoted with red discs.

Extended Data Table 1 | Timing properties and age estimates

	PSR J0205+6449	PSR B2334+61	CXOU J0852–4617
Class	RPP	RPP	CCO
assoc./nick	3C 58	SNR G114.3+0.3	SNR Vela Jr
d [kpc]	2.0 ± 0.3^a	$3.1_{-1.0}^{+0.2b}$	$0.5 - 1^c$
P [s]	$0.06565923(2)^d$	$0.495228(3)^e$	-
\dot{P} [$\times 10^{-13}$ s/s]	1.935 ± 0.003^d	1.9098 ± 0.0003^f	-
\dot{E}_{rot}^\dagger [$\times 10^{34}$ erg/s]	2666	6.1	-
B_p^\ddagger [$\times 10^{12}$ G]	7.2	19.7	-
τ_c [kyr]	58.8	41.1	-
τ_r [kyr]	$0.80^{g,*}$	$7.7 \pm 0.8^{h,**}$	$2.5 - 5.0^c$

^a: Rotational energy loss, $\dot{E}_{rot} = 3.9 \times 10^{46} \dot{P}/P^3$ erg/s; ^b: Magnetic field strength at the pole, assuming that rotational energy losses are dominated by dipolar magnetic torques, $B_p = 6.4 \times 10^{10} (PP)^{1/2}$ G. ^{*}: A conservative 10% error was adopted only in the analysis and Fig. 1, despite the date was inferred for the actual detection of the supernova. ^{**}: A conservative 10% error was adopted in this case to account for any systematics in the SNR age characterization reported in ref. 20. Distance and age references: a: ref. 41, b: ref. 44, c: ref. 21, d: ref. 66, e: ref. 67; f: ref. 68; g: ref. 19, h: ref. 20.

Extended Data Table 2 | Spectral analysis results

Parameters	PSR J0205+6449	PSR B2334+61	CXOU J0852
Model	BB+PL	BB	BB
N_{H} ($\times 10^{22}$ cm $^{-2}$)	$0.49^{+0.08}_{-0.05}$	0.20^{ϕ}	0.47 ± 0.04
Γ	$1.51^{+0.07}_{-0.06}$	-	-
kT_{bb} (keV)	$0.20^{+0.08}_{-0.04}$	0.16 ± 0.01	0.397 ± 0.009
R_{bb} (km)	$0.6^{+1.5}_{-0.3}$	$0.9^{+0.7}_{-0.6}$	0.24 ± 0.08
χ^2_{ν} (d.o.f.)	0.96 (598)	-	1.13 (143)
C-stat (d.o.f.)	-	6.46 (12)	-
F_{th} (10^{-13} erg cm $^{-2}$ s $^{-1}$)	$3.02^{+0.79}_{-0.61}$	0.68 ± 0.10	$25.9^{+1.1}_{-1.0}$
kT_{cool} (keV)	$< 4 \times 10^{-3}$	$< 4 \times 10^{-2}$	$< 5 \times 10^{-2}$

ϕ : Kept frozen during the fits. Quoted errors reflect 90% confidence levels. See uncertainty propagation analysis in Section ‘Predictions accounting for the uncertainty on the luminosity’ for the L_{th} of two of the sources ('). The reported best-fit parameters have been obtained assuming absorption tables by ref. 48.

Extended Data Table 3 | Log of the XMM-Newton and Chandra observations

Source	Date Obs.	Obs.ID	Satellite	Exp. [ks]	Cts. [10^3]	Refs.
PSR J0205+6449	2003-04-22	4383	<i>Chandra</i>	38.7	4.82 ± 0.07	45
	2003-04-23	4382		167.4	22.05 ± 0.15	45
	2003-04-26	3832		135.8	17.72 ± 0.13	45
PSR B2334+61	2004-02-12	0204070201	XMM	26.8	0.32 ± 0.02	44
CXOU J0852–4617	2001-09-17	1034	<i>Chandra</i>	31.4	9.5 ± 0.1	37

Exposure times and counts for the three sources.

Extended Data Table 4 | Spectral analysis for the atmosphere model

Parameters	PSR J0205+6449	PSR B2334+61	CXOU J0852
Chemical composition: H			
kT_{eff} (keV)	0.19±0.04	0.12±0.03	0.31±0.01
N_{nsmaxg}^{ψ} (10^{-3})	$3.0^{+3.0}_{-1.0}$	70^{+70}_{-30}	$2.1^{+0.6}_{-0.4}$
F_{th} (10^{-13} erg cm $^{-2}$ s $^{-1}$)	0.70 ± 0.10	0.80 ± 0.10	27.0 ± 0.5
Chemical composition: C			
kT_{eff} (keV)	0.20±0.03	0.10±0.01	
N_{nsmaxg}^{ψ} (10^{-3})	$2.0^{+3.0}_{-1.0}$	20^{+4}_{-1}	
F_{th} (10^{-13} erg cm $^{-2}$ s $^{-1}$)	0.80 ± 0.20	0.56±0.07	-
Chemical composition: O			
kT_{eff} (keV)	0.36±0.13	0.25±0.02	
N_{nsmaxg}^{ψ} (10^{-3})	$0.14^{+0.12}_{-0.06}$	31^{+14}_{-10}	
F_{th} (10^{-13} erg cm $^{-2}$ s $^{-1}$)	$0.70^{+0.12}_{-0.05}$	0.68 ± 0.10	-

All fits were performed assuming $B=10^{12}$ G and fixing the distance to the values reported in Extended Data Table 1; ψ : Kept frozen during the fits. ψ : $N_{\text{nsmaxg}} = (R_{\text{em}}/R_{\text{NS}})^2$.

Extended Data Table 5 | Classification probabilities in 4D

PSRB2334+61		PSRJ0205+6449	
I. FIVE BEST MODELS AND THEIR CLASSIFICATION PROBABILITIES			
GM1A, $1.6 M_{\odot}$, 2×10^{13} G	0.1980	BSK24, $1.6 M_{\odot}$, 7×10^{12} G	0.1203
BSK24, $1.8 M_{\odot}$, 1×10^{13} G	0.1641	BSK24, $1.8 M_{\odot}$, 2×10^{13} G	0.0857
BSK24, $1.8 M_{\odot}$, 2×10^{13} G	0.1087	BSK24, $1.6 M_{\odot}$, 5×10^{12} G	0.0755
BSK24, $1.8 M_{\odot}$, 3×10^{13} G	0.0651	BSK24, $1.6 M_{\odot}$, 1×10^{13} G	0.0723
BSK24, $1.8 M_{\odot}$, 7×10^{12} G	0.0629	BSK24, $1.6 M_{\odot}$, 3×10^{12} G	0.0696
II. EQUATION OF STATE			
BSK24	0.5323	BSK24	0.5409
GM1A	0.4265	GM1A	0.4054
SLy4	0.0413	SLy4	0.0537
III. MASS (M_{\odot})			
1.4	0.0101	1.4	0.1226
1.6	0.3512	1.6	0.5682
1.8	0.6387	1.8	0.3092
IV. B_p (G)			
1×10^{12}	0.0000	1×10^{12}	0.0157
3×10^{12}	0.0082	3×10^{12}	0.2136
5×10^{12}	0.0544	5×10^{12}	0.1813
7×10^{12}	0.0725	7×10^{12}	0.2806
1×10^{13}	0.2674	1×10^{13}	0.2015
2×10^{13}	0.4195	2×10^{13}	0.1072
3×10^{13}	0.1476	3×10^{13}	0.0001
5×10^{13}	0.0304	5×10^{13}	0.0000
7×10^{13}	0.0000	7×10^{13}	0.0001

For the two sources PSR B2334+61 and PSR J0205+6449, the five most probable models in the 4D space, sorted by their classification probability (panel I), as well as the marginalised probabilities of the considered EoSs, and values for the mass and magnetic field (panels II–IV). The highest marginal probabilities are denoted with bold typeface.